


# HIGH-FIDELITY DATASET-BASED SHAPE AND STRUCTURE OPTIMIZATION FOR AIRCRAFT DESIGN

Markus Maier[1,2], Kaare Sørensen-Libik[2], Ögmundur Petersson[2] & Christian Breitsamter[1]

[1]Chair of Aerodynamics and Fluid Mechanics, Technical University of Munich
[2]Airbus Defence and Space GmbH

## Abstract

Automatic numerical optimization is a primary enabler of efficient multidisciplinary aircraft design across civil and military sectors. This work demonstrates the extension of high-fidelity dataset-based aerodynamic shape optimization into the structural domain using the OTIFAN (Optimization Test Interceptor with ducted Fan) configuration. An automated framework transfers the rigid, high-fidelity aerodynamic loads to a structural optimizer, enabling automated structural mass minimization based on analytic gradients from the linear finite-element method. The wall thicknesses of key structural members - specifically the wing spars, ribs and skin - are sized to minimize the total mass. Structural integrity is ensured across the flight envelope and for off-design regions by imposing strict stress constraints. To account for structural stability, a knockdown factor is applied to mitigate the omission of explicit buckling constraints. Compared to a square-cube law mass assumption, this high-fidelity computational structural mechanics approach achieves 5 % to 29 % total weight savings, reducing mass property uncertainties and enhancing mission-level performance. Ultimately, this paper demonstrates the utility of dataset-based optimization of external shape and load-bearing structures, using shared high-fidelity data across disciplines to accelerate the operational maturity of future aircraft designs.

**Keywords:** High-fidelity dataset-based optimization; Shape and structure optimization; Mission performance; Stability and control; Aircraft design.

## Nomenclature

| | | | |
|---|---|---|---|
| AM | Additive manufacturing | HPC | High-performance computing |
| CAD | Computer-aided design | MDO | Multidisciplinary Design Optimization |
| CFD | Computational fluid dynamics | OTIFAN | Optimization Test Interceptor w. ducted Fan |
| CSM | Computational structural mechanics | PLA | Polylactic acid |
| EDF | Electric ducted fan | RANS | Reynolds-Averaged Navier-Stokes |
| EI | Expected improvement | RF | Reserve factor |
| FE | Finite Element | SA | Spalart-Allmaras |
| FEM | Finite Element method | SF | Factor of safety |
| FOM | Figure of merit | SQL | Square-cube law |
| FSI | Fluid-structure interaction | UAV | Unmanned aerial vehicle |
| GFEM | Global finite element model | ULF | Ultimate load factor |

## 1. Introduction

The design process for commercial and military aircraft is inherently multidisciplinary, requiring accurate data of multiple physical domains to achieve viable configurations [1]. Among these, aerodynamics and structural mechanics are two of the most sensitive and interdependent disciplines.

In recent decades, continuous advancements in numerical algorithms and high-performance computing (HPC) hardware have matured Computational Fluid Dynamics (CFD) and Computational Structural Mechanics (CSM). These methods enable the detailed assessment of aerodynamic and structural characteristics for full aircraft configurations. However, available numerical methods span a wide range of fidelity levels and computational costs, which are typically inversely related. Furthermore, the choice of aero-structural coupling strategy significantly impacts the overall computational cost and turn-around time.
Since aircraft are designed to operate across a wide range of operating conditions, or flight envelope, multiple analyses applying these computational methods have to be performed. The analysis results for these operating conditions are stored in a dataset, describing the characteristics of the aircraft configuration. A flight envelope for commercial and especially military aircraft covers multiple dimensions including Mach number, flow angles and control settings. Additionally, the boundary regions expose highly non-linear flow physics (such as shock-induced separation and vortex interactions) that must be resolved more densely, resulting in a dataset containing a large number of flight conditions and control deflections.

Consequently, aircraft designers must carefully balance the selection of high-fidelity methods, coupling strategies, and dataset resolution against available computational resources and project timeframe. To ensure acceptable engineering turn-around times, an automated multidisciplinary design optimization (MDO) framework leveraging HPC resources is essential.

## 1.1 Motivation

External aerodynamic loads constitute a large part of the dimensioning sizing loads for commercial aircraft, but even more so for military vehicles with high agility requirements such as fighters or (unmanned) interceptors. By including the structural domain inside an optimization workflow via finite-element (FE) models of the structural members, the latter can be sized to the corresponding load cases, yielding a numerically validated structure in tandem to the validated shape. This sequential approach yields reliable mass property estimates based on high-fidelity aerodynamic load distributions and structural responses, ultimately ensuring greater accuracy in mission performance as well as in stability and control evaluations.

## 1.2 State of the Art

Reynolds-averaged Navier-Stokes (RANS) CFD simulations are considered the state of the art high-fidelity method for aerodynamic analysis in industrial applications. When applied to complex, full-aircraft geometries, RANS methods provide sufficient accuracy even within flow regimes governed by non-linear phenomena like flow separation [2, 3]. Furthermore, recent developments enable the production of high-fidelity aerodynamic datasets in reasonable time frames for industrial applications [4].
The finite-element method (FEM) is the established standard for high-fidelity CSM simulations to analyze the behavior of structures under mechanical loads [5, 6, 7]. Especially the linear form is widely applied due to its relevance for certification and design rules, as well as the fast turn-around times on modern computers. Crucially, the limited additional cost for fully analytic derivatives renders it the preferred choice for the efficient gradient-based structural optimization of complex geometries such as aircraft structures [8].
Despite these individual disciplinary advancements, seamlessly coupling high-fidelity CFD with high-fidelity CSM inside an MDO framework, that targets a robust design across the flight envelope remains a subject of active research.

## 1.3 Research Gap

While recent literature indicates that routine application of high-fidelity, dataset-based aircraft optimization is becoming computationally feasible, current frameworks still exhibit critical limitations [9]: The current state of the art in high-fidelity aircraft shape optimization is largely focused on major airframe components, such as wings [10, 11, 12], and frequently neglects propulsive effects [10, 13, 14].

Moreover, even when multiple design points are considered, off-design conditions and critical envelope corners are often omitted, potentially compromising the operational robustness of the final design [7, 13, 15].

To bridge these gaps, this paper presents an automated MDO framework that considers the complete aircraft configuration, including the propulsion system during the shape optimization, while optimizing the wing structure in an integrated loads loop. The core contributions of this work are:

- The generation of a comprehensive aerodynamic dataset using high-fidelity (RANS) CFD for the rigid full aircraft configuration across a multi-dimensional flight envelope.
- The automated mapping of these high-fidelity rigid aerodynamic loads to a detailed structural model for sizing of the primary wing structure using the efficient, gradient-based optimization tool LAGRANGE.
- The integration of low-fidelity disciplinary modules to evaluate mission performance under realistic stability and control constraints using the high-fidelity derived mass properties.

The resulting framework provides an advanced level of multidisciplinary completeness and accuracy, ensuring consistent aerodynamic and structural assessment across the entire operational envelope.

## 2. Methodology

This work is based on the high-fidelity dataset-based shape-optimization framework presented by Maier et al. [9], which has been significantly expanded in this study.
In addition to the high-fidelity treatment of the aerodynamics, the key structural component - the wing - is now analyzed via a high-fidelity CSM method, specifically the finite element (FE) method. The structural loads are extracted from the high-fidelity aerodynamic data and supplemented by additional operational load cases. The thickness of the wing shell patches, ribs, and spars is iteratively optimized to yield a viable structure at minimum weight while complying with material stress constraints. Detailed insight into the methodology is given in the following sections.

### 2.1 Framework

An overview of the optimization workflow, orchestrated by an automated *Python* programme is given in Figure 1.
The framework instructs a computer-aided design (CAD) suite to update a parametric CAD model, and subsequently exports the resulting surface geometry and an FE model. As detailed in [9], the updated geometry is utilized in an automated meshing process, and the meshes are solved for flow conditions and control settings covering the flight envelope of the current configuration. The framework extension introduced in this work includes a specialized module termed the *Loads Cutter*. Based on the updated geometry information, it post-processes the CFD surface solutions to derive data-efficient zonal and integral load coefficients. The integrated structural optimizer reads the updated FE model and minimizes the mass $m$, by adjusting the design parameters $x$ - the thickness of structural members - under the rigid loads introduced, while considering structural design constraints $g(x)$. The inputs are prepared by the framework, which also evaluates the resulting mass properties within the shape optimization objective, i.e., the design missions. Ultimately, the next set of shape parameters is selected based on the chosen optimization strategy.

### 2.2 Test Case

The framework is applied to a simplified yet physically relevant test case as introduced by Maier et al. [9]: The OTIFAN (**O**ptimization **T**est **I**nterceptor with ducted **F**an) configuration represents an expendable, subsonic unmanned aerial vehicle (UAV), designed for catapult launch and fast intercept missions against low-flying subsonic targets.

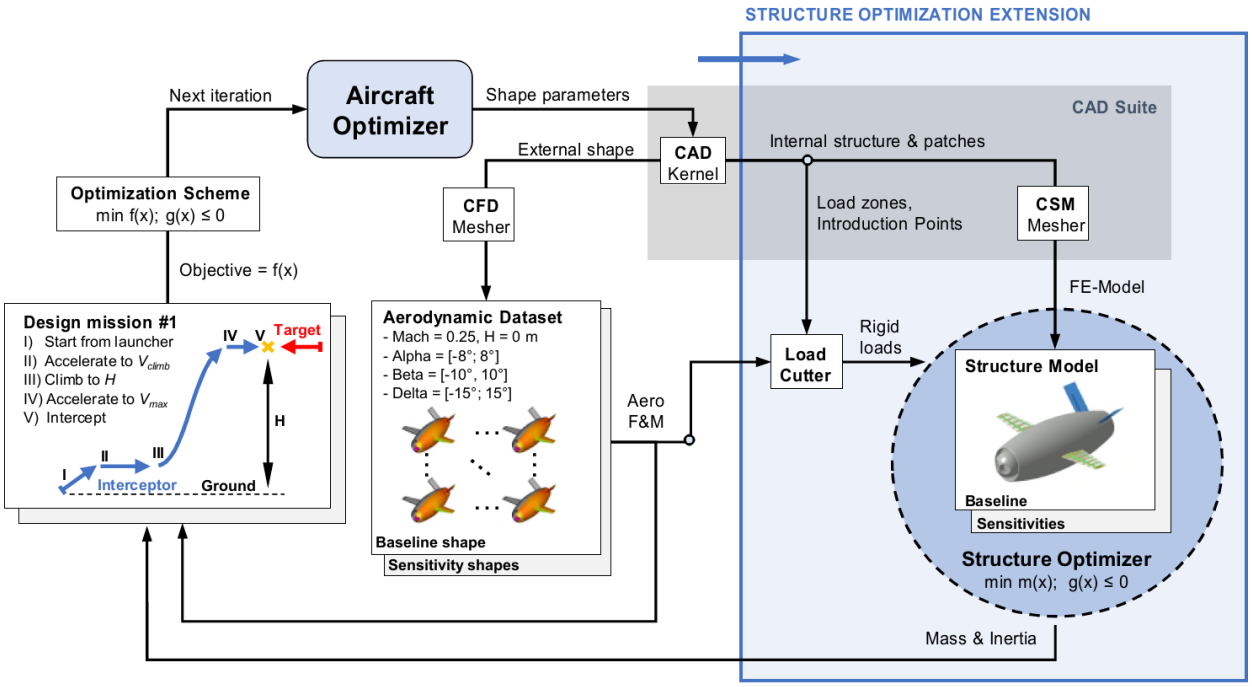



Figure 1 – Overview of the optimization workflow. Extension for structural optimization in blue.

The configuration features an axisymmetric fuselage that houses a sensor head, batteries, control systems, and an internally mounted electric ducted fan (EDF) propulsion system. The wing has a $5^\circ$ incidence, while the all-movable, rectangular V-tail is inclined at a $45^\circ$ dihedral angle. Wing and tail use symmetric NACA 64-010 airfoils, which have been modified to a trailing edge thickness of 1 % of the local chord length.

A three-view of the parametric CAD model, including the design parameters, their respective bounds, and an overview on the mass model is shown in Figure 2, while the technical specifications are provided in Table 1.

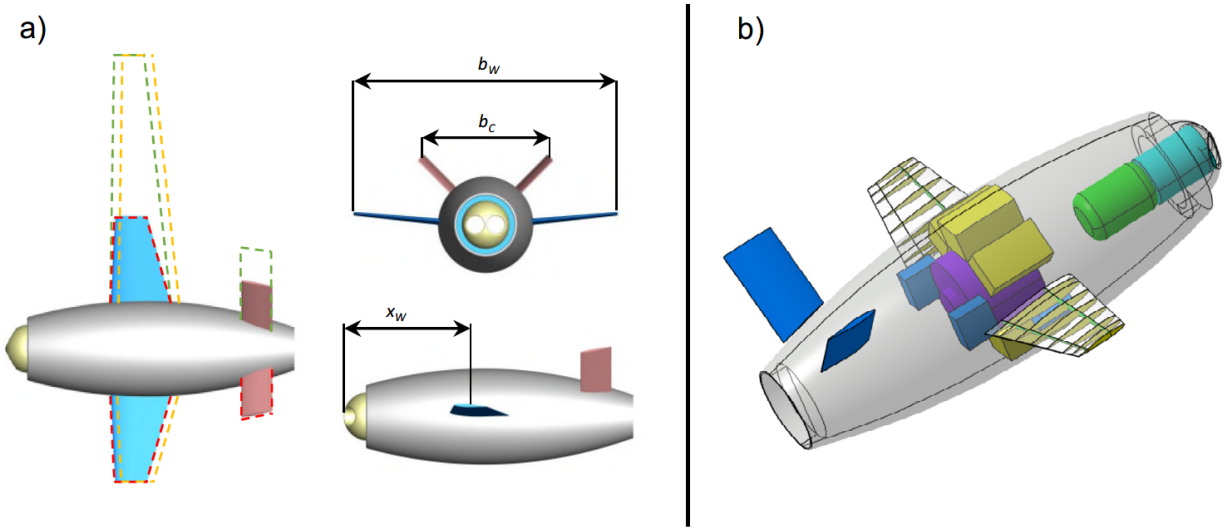



Figure 2 – Parameterized CAD model of the OTIFAN configuration. A) Three-view including the design parameters and their respective bounds [9]. B) Overview of the mass model including the mass dummies for various systems.

Table 1 – OTIFAN configuration specifications. [9]

| Specification | Value | Unit |
|---|---|---|
| Altitude range | 0 ... 2000 | [m] |
| Mach range | 0.05 ... 0.25 | [−] |
| Take-off mass | $\sim 3.0$ | [kg] |
| Propulsion type | Internal 90 mm EDF | |
| Batteries | 4x Li-Po 6S, 1.6 Ah @ 80C | |
| Gross thrust | 38 (static, uninstalled) | [N] |
| Flight time | 118 | [s] |
| Fuselage length | 0.545 | [m] |
| Fuselage max dia | 0.180 | [m] |
| Wing long. position | 0.2 ... 0.3 | [m] |
| Wing surface area | 0.05 ... 0.20 | [$m^2$] |
| Wing root chord | 0.140 | [m] |
| Wing tip chord | 0.060 | [m] |
| Wing span | 0.5 ... 2.0 | [m] |
| V-tail span | 0.175 ... 0.275 | [m] |

## 2.3 CFD setup

The applied CFD setup aligns with the methodology in [9].

The meshing routine creates unstructured, hybrid, vertex-centered dual cell grids. Prism layers are extruded from a triangular surface mesh and subsequently merged into a surrounding tetrahedral volume mesh. Local refinements are placed in regions with high-curvature features, such as the leading and trailing edges, as well as in regions where high flow gradients are occurring. The deflection of control surfaces is handled efficiently via the Chimera approach [16] by modeling the surfaces as sub-meshes. A robust interpolation method allows for the rotation of each sub-mesh around its respective hinge line during runtime. Details of the applied mesh are provided in Figure 3.
The compressible RANS equations are solved via the DLR TAU-Code [17]. The solver input is prepared on a local workstation by the dataset generation pipeline, while the computational workload is shifted to an HPC cluster in highly parallelized manner.
Due to its efficiency, robustness and accuracy for external aircraft aerodynamics [18], the one-equation Spalart-Allmaras (SA) turbulence model with the Edward's modification [19] and active rotation correction is applied.

The flight envelope for the OTIFAN configuration spans the dataset dimensions specified in Table 2. It includes off-design operating conditions with respect to the Angle of Attack ($\alpha$), as stall generally occurs around $\alpha = 6^\circ$ on this configuration, as well as the deflection of the V-tail ($\delta$). The selected range of $\delta$ captures regions characterized by a negative pitch control power gradient. Propulsive effects are included by modeling the EDF using an engine deck and boundary conditions derived from explicit simulations of the rotating fan inside the fuselage. Further details can be found in [9].

## 2.4 CSM setup

For the initial demonstration of this methodology, the structural representation is limited to one wing of the OTIFAN configuration, which is modeled via a detailed 3D FE shell model. To replicate realistic root clamping conditions, a segment of the fuselage, hereafter referred to as the "stub," is included. The thickness of the wing components spars, ribs and shell patches is optimized to yield the lightest aircraft structure, able to withstand the operational loads for all relevant flight conditions and during the launch phase.

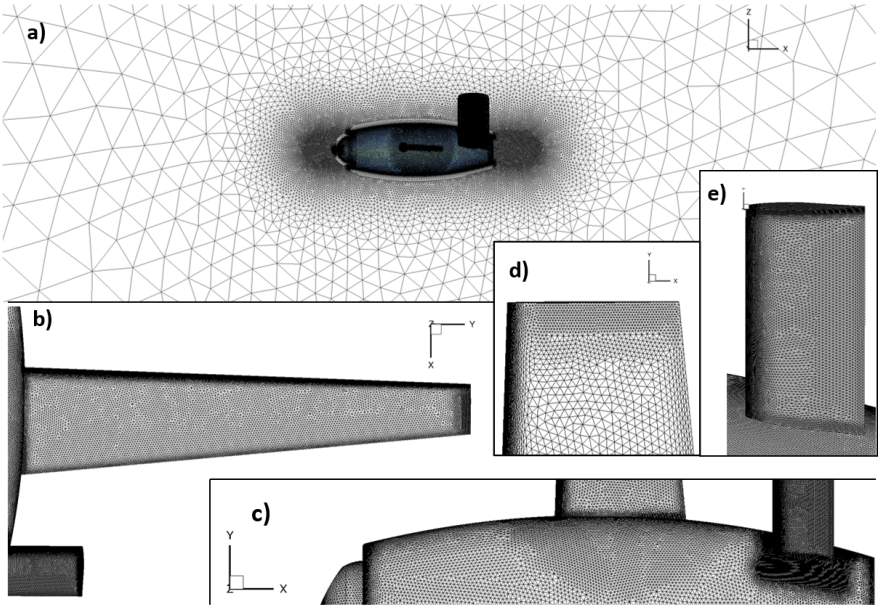



Figure 3 – Mesh used for the OTIFAN optimization showing the farfield a) and details of the wing b), the fuselage c), the wing tip d) and the V-tail e).

Table 2 – OTIFAN aerodynamic dataset dimension ranges.

| Dimension | Range | Unit |
|---|---|---|
| Altitude range | $0 \ldots 2000$ | $[\mathrm{m}]$ |
| Mach range | $0.05 \ldots 0.25$ | $[-]$ |
| Alpha range | $-8.0 \ldots +8.0$ | $[^\circ]$ |
| Delta range | $-15.0 \ldots +15.0$ | $[^\circ]$ |

The FE model is automatically generated for each shape variation using the *CATIA V5 Advanced Meshing Tool*. An overview of the FE mesh for the midpoint design including a component breakdown is presented in Figure 4.

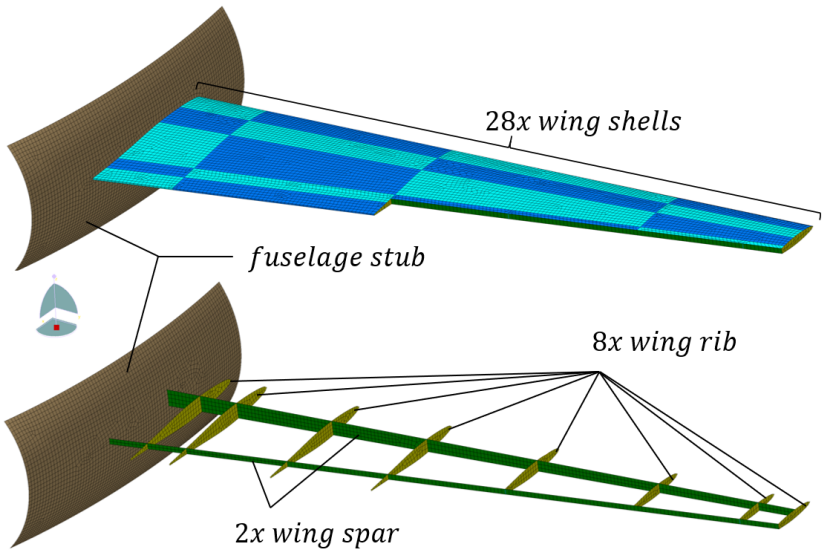



Figure 4 – Finite element model representing the fuselage stub (brown), the two spars (green) the eight ribs (yellow), as well as the 28 shells (blue) for the midpoint design.

An overview of the load mapping sequence from the CFD results to the FE model is provided in Figure 5.

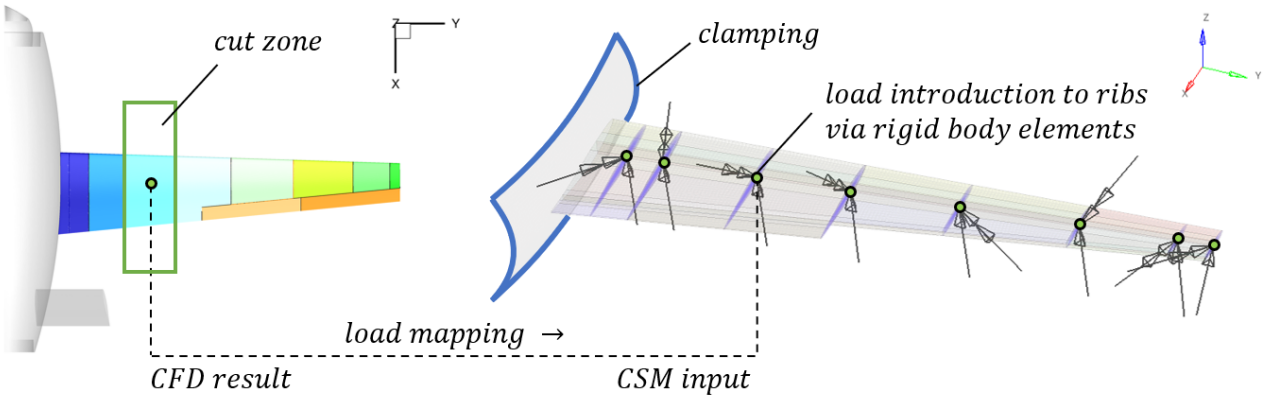



Figure 5 – Load transfer from CFD result to CSM. Represented via force vectors (single arrow) and moment vectors (double arrow) into the ribs. The fuselage stub is clamped at the boundary.

The applied aerodynamic loads are extracted from the CFD surface solutions utilizing adaptive cut zones. Surface pressure and viscous forces are integrated on the surface zones with respect to a dedicated reference point. These zonal loads are subsequently applied to the structural model at the respective load introduction points and from there on distributed to the respective FE mesh component elements. For this specific test case, the aerodynamic cut loads are distributed into the internal wing ribs using rigid body elements.

For the structural sizing loop, the Airbus in-house optimization tool *LAGRANGE* [8] is integrated directly into the shape optimization framework. *LAGRANGE* is capable of simultaneously managing numerous independent design variables, such as element thicknesses and ply orientations for anisotropic laminates, while enforcing a diverse set of stress, displacement, or buckling constraints via highly efficient gradient-based algorithms. Especially when sizing thin walled structures, the sensitivity to buckling must be respected.
The FE model is parsed, the clamping is applied to the boundary nodes of the fuselage stub by constraining all translational degrees of freedom ($u_x = u_y = u_z = 0$). To eliminate nonphysical local boundary artifacts from biasing the optimization routine, the fuselage stub is assigned a constant, non-design thickness of $4\,\mathrm{mm}$, and its stress is not monitored by the optimizer.
The load cases are comprised of the $10\mathrm{g}$ acceleration case during the catapult launch and the aerodynamic loads for all flight conditions of the dataset. The latter are queried from the aerodynamic dataset for the zonal coefficients of the starboard zones under the computed flow conditions and control settings. Load introduction points, the rigid body elements, and the load cases are generated fully autonomously by the Python framework.
In this demonstration on the OTIFAN configuration, the flaperon surface loads are directly mapped to rib 5 and rib 6 respectively. A more detailed loads mapping including hinges and actuators can easily be integrated in an industrial application as shown by Reinbold [6]. The coefficients are transformed into load and moment vectors at the conservative conditions of the nominal Mach number $Ma = 0.25$ at mean sea level.

The manufacturing process is assumed to be additive manufacturing (AM) and Polylactic Acid (PLA) is selected as material for the wing structure. Table 3 summarizes the isotropic mechanical properties utilized in this study as given in [20].
To ensure a reliable and physically viable wing structure under the given load envelope, sizing optimization constrains the operational stress levels across all internal and external wing elements to maintain a local Reserve Factor ($RF$) strictly greater than unity, as defined in Eq. 1:

$$RF = \frac{\sigma_{\text{HVM,mat}} \cdot KF_{\text{buck}}}{\sigma_{\text{HVM,max}} \cdot SF_{\text{dyn}} \cdot ULF} > 1.0 \tag{1}$$

Table 3 – Material properties for PLA.

| Property | Value | Unit |
|---|---|---|
| Young's modulus | 3500 | [MPa] |
| Poisson's ratio | 0.35 | [−] |
| Density | 1300 | [kg/m$^3$] |
| Ultimate Tensile strength | 50 | [MPa] |

The Hencky-Von-Mises equivalent stress allowable for the wing structure is set to $\sigma_{\text{HVM,mat}} = 50\,\text{MPa}$ and is compared to the maximum Hencky-Von-Mises equivalent stress under the given load cases $\sigma_{\text{HVM,max}}$. The safety factor for dynamic overshoots from the quasi-steady aerodynamics is set to $SF_{\text{dyn}} = 1.\overline{3}$, and the ultimate load factor applied is $ULF = 1.5$. Furthermore, a knockdown factor for buckling $KF_{\text{buck}} = 0.25$ is compensating for the neglected buckling constraints, which are not yet automated in the shape optimization framework. Since AM allows for great design freedom, the only manufacturing constraint applied is a minimum wall thickness.

Compared to the high-fidelity aerodynamic CFD simulations, the one-directional CSM sizing based on the rigid loads is computationally inexpensive and adds only negligible computational costs to the shape optimization loop. In contrast, utilizing a fully coupled aero-elastic optimization approach, such as the method proposed by Reinbold [6], would result in a three- to five-fold increase in the total computational cost.

Once the structural optimization converged to a valid minimum mass design, the final wing structural mass is extracted by the framework and summed directly to the fixed mass of the configuration, affecting the flight performance in the maneuvering analysis performed inside the objective evaluation. Elastic effects are neglected by the objective function.

## 2.5 Objective

The objective for the shape optimization is composed of two design missions, which are rated and weighted in alignment with [9].
While the primary mission represents a target interception at maximum height $H$ initiated by a catapult launch as illustrated in Figure 6, the secondary mission represents a contingency scenario. In case the target is missed at the end of the primary mission, the vehicle flies an inverted intercept following a half-loop maneuver as shown in Figure 7.

The rating of each mission is performed based on the respective figures of merit (FOMs) and constraint penalties. Each FOM value is scaled across three reference points corresponding to $0$, $100$ and $200$ mission points (pts), while the constraint values are scaled across three reference points corresponding to $105\,\%$, $95\,\%$ and $0\,\%$.
Tables 4 and 5 detail the FOMs, the constraints, the respective scaling values and the weights for the primary and secondary mission, respectively.

The primary mission time is 80 % of the total flight time and includes the catapult launch from an $8\,\text{m}$ rail. The launch velocity is set to A +5 % of the nominal stall speed $1.05\,V_S$, which is achieved by constant acceleration from $V_0 = 0\,\text{m/s}$. The stall speed $V_S$ is evaluated from the dataset as minimum velocity in trimmed level flight. Structural integrity during the launch is ensured by constraining the axial load factor to $n_{xb} < 15\,\text{g}$, and applying this inertia load case to the structural optimization.

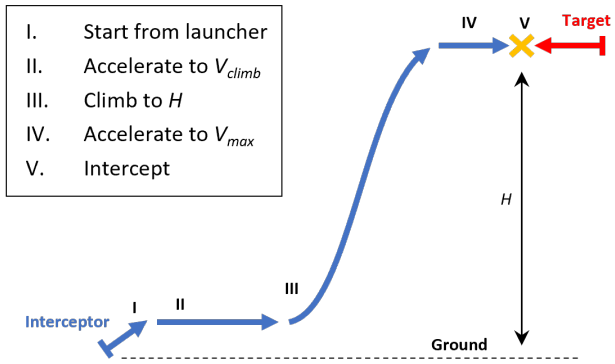



Figure 6 – Primary mission profile.

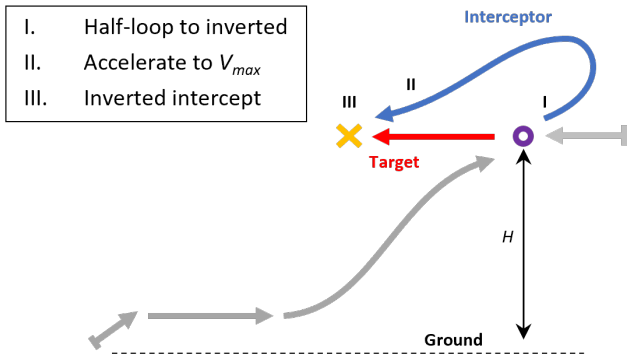



Figure 7 – Secondary mission profile.

Table 4 – Primary mission metrics.

| **FOMs** | **Scaling** $[0, 100, 200]$ $pts$ | **Weight** |
|---|---|---|
| $H$ | $[500, 1000, 2000]$ m | 3 |
| $J$ | $3\,\text{kg} \cdot [0.1, 0.2, 0.3] \cdot 340\,\text{m/s}$ | 1 |
| **Const.** | **Scaling** $[105, 95, 0]$ % | **Weight** |
| $n_{xb}$ | $[0, 10, 15]$ g | 4 |

Table 5 – Secondary mission metrics.

| **FOMs** | **Scaling** $[0, 100, 200]$ $pts$ | **Weight** |
|---|---|---|
| $t_{inv}$ | $t_{inv}(n_{zb} = [1.5, 2.5, 9.0]\,\text{g})$ | 1 |
| $V_{tgt}$ | $[50, 150, 200]$ km/h | 3 |
| **Const.** | **Scaling** $[105, 95, 0]$ % | **Weight** |
| $n/a$ | $n/a$ | $n/a$ |

The climb segment is fixed to 80 % of the primary mission time, at maximum rate of climb $ROC$ to maximize the altitude $H$ as specified in Equation 2.

$$H = ROC \cdot 0.8^2 \cdot t_{max} \tag{2}$$

$ROC_{max}$ is determined by evaluating the dataset for the highest value of the specific excess power $SEP$ in trimmed level flight.

$$SEP = V \cdot n_{xg} = ROC \tag{3}$$

The remainder of the primary mission is for acceleration to the terminal velocity at trimmed flight $V_{max}$, which is evaluated from the dataset to retrieve the maximum terminal impulse $J_{max}$.

The remaining 20 % of the total flight time is set aside for the secondary mission, including the half-loop maneuver, which enables a second intercept attempt in inverted flight. The minimal time to inverted $t_{inv}$ is identified by the highest normal load factor $n_{z,b}$ at trimmed pitching moment. The respective flight condition is assumed during the half-loop as given in Equation 4. A factor of two is applied to account for the quasi-steady modeling. The maximum velocity of the target $V_{tgt}$, which can still be intercepted, is computed at $V_{max}$ in trimmed level flight, which is assumed to be close to $V_{max}$ at inverted level flight as given in Equation 5.

$$t_{inv} = \frac{\pi \cdot V_{xb,\,pu}}{g \cdot (n_{zb,\,pu} - 1)} \cdot 2 \tag{4}$$

$$V_{tgt} = \frac{V_{max}}{1 + \frac{t_{inv}}{0.2 \cdot t_{max}}} \tag{5}$$

The rating per mission is computed as the weighted sum of the respective rated FOMs, multiplied with the weighted product of the rated constraints acting as dampers as stated in Equation 7. Prior to computing the mission rating, the FOMs and constraints are normalized per mission as specified in Equation 6.

Ultimately, the multi-mission objective is computed as weighted sum of the mission ratings $mr_i$ as stated in Equation 8, where the mission weighting is 4:1 between the primary and the secondary mission.

$$\overline{w}_i = \frac{w_i}{\sum w} \tag{6}$$

$$mr(\vec{x}) = \left(\sum fr_i(\vec{x}) \cdot \overline{w}_i\right) \cdot \left(\prod cr_j(\vec{x}) \cdot \overline{w}_j\right) \tag{7}$$

$$obj(\vec{x}) = \sum mr_i(\vec{x}) \cdot \overline{mw}_i \tag{8}$$

## 3. Results

For the demonstration of the extended shape optimization on the OTIFAN configuration, the grid search method was chosen as optimization strategy. As the execution is decoupled from the objective, efficient re-processing of the candidate pool is enabled in case of objective function updates.

The shape optimization history is given in Figure 8. It shows the resulting objective, the ratings of the primary and secondary missions $mr_1$ and $mr_2$, as well as the three shape parameters of wing position $x_w$, wing span $b_w$ and span of the V-tail $b_c$, each normalized to their respective bounds. The bounds can be found in Table 1. Each iteration passed the complete workflow as detailed in subsection 2.1.

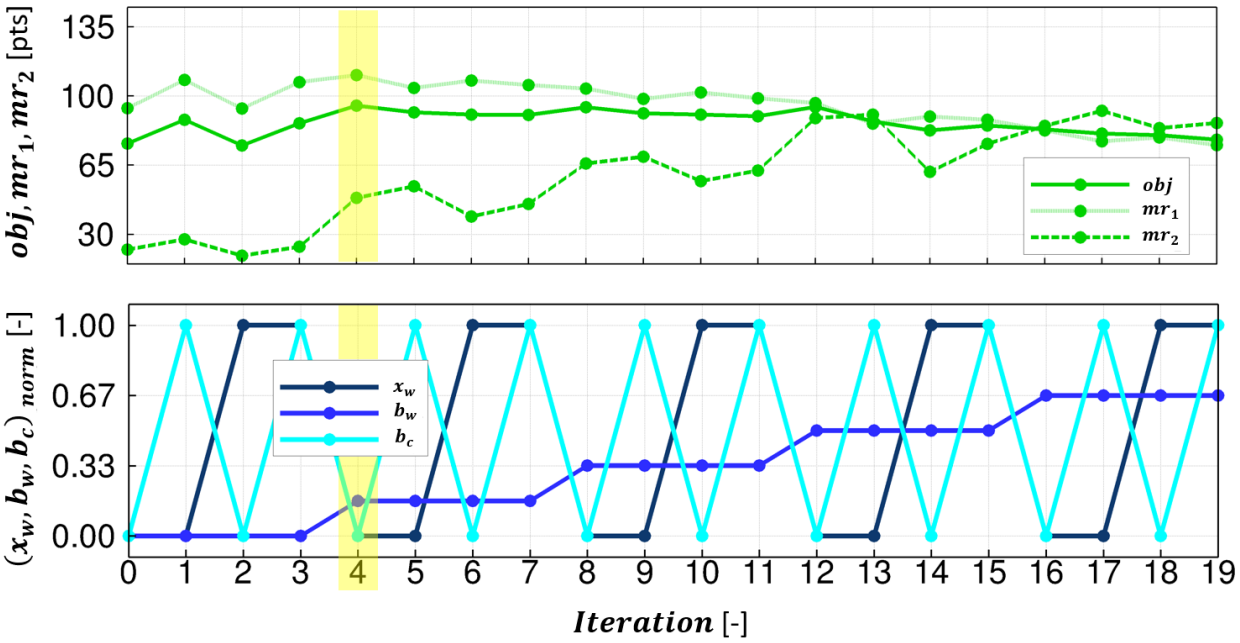



Figure 8 – Optimization history of the grid search method, showing the objective and mission ratings $obj$, $mr_1$ and $mr_2$, alongside the associated normalized shape parameters of wing position $x_w$, wing span $b_w$ and V-tail span $b_c$.

The best-performing candidate is identified in iteration four, yielding an objective rating of $obj = 96$ points. At this rating, the wing position $x_w$ and the V-tail span $b_c$ are at their lower bounds, while the wingspan has reached the second grid point.
Overall the objective function is relatively flat. For the majority of the wing span range, the primary mission rating exceeds the secondary mission rating. The primary mission is adversely affected by a larger V-tail span and a more aft wing position. Conversely, the secondary mission increases with a larger wingspan, while the wing position has only a secondary effect. The weakest overall effect is observed from the tail span.

A comparison of the best candidate configuration versus the midpoint design is given in Table 6.

Table 6 – Comparison of the midpoint versus the best candidate OTIFAN configuration.

| Property | Midpoint | Best candidate | Unit |
|---|---|---|---|
| $obj$ | 86 | 90 | [pts] |
| $x_w$ | 0.218 | 0.208 | [m] |
| $b_w$ | 1.250 | 0.750 | [m] |
| $b_c$ | 0.225 | 0.175 | [m] |
| $mr_1$ | 87 | 107 | [pts] |
| $mr_2$ | 84 | 52 | [pts] |
| $cr_1$ | 100 | 98 | [%] |
| $mass$ | 3.014 | 2.904 | [kg] |
| $H$ | 949 | 1167 | [m] |
| $J$ | 180 | 193 | [N · s] |
| $n_{xb}$ | 4.6 | 7.4 | [$g$] |
| $t_{inv}$ | 9.6 | 14.7 | [s] |
| $V_{tgt}$ | 109 | 99 | [km/h] |

Even though the objective function is relatively flat with the optimized wing structure, the performance was increased by four points. The best candidate configuration is $110$ g lighter and reaches a higher primary mission rating, whereas the secondary mission rating is decreased. For the primary mission, a higher target altitude $H$ and terminal impact impulse $J$ are achieved, while the constrained axial load factor during launch $n_{xb}$ remains inactive for both configurations. For the secondary mission, both figures of merit (FOMs) - the time to inversion $t_{inv}$ and the maximum target speed $V_{tgt}$ - are reduced to the benefit of the primary mission FOMs.

The zero control characteristics of the aerodynamic datasets for the two configurations are presented in Figure 9. Note that the reference dimensions for the aerodynamic coefficients are fixed for the optimization.

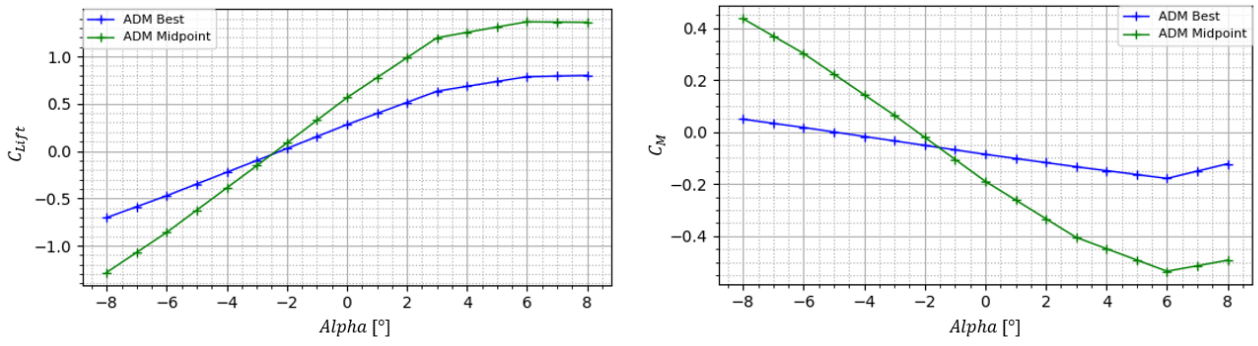



Figure 9 – Comparison of zero control integral aerodynamic coefficients for the midpoint and best candidate designs.

From the zero control polars, it can be seen that both datasets enclose the challenging region of maximum lift $C_{Lift,max}$, marking the onset of flow detachment. While the midpoint design has a higher lifting capability, this metric is not prioritized by the design mission. The pitching moment coefficient slope $\frac{dC_M}{d\alpha}$ moment appears three to five times more steep, resulting in a higher requirement for control deflection or a larger V-tail surface area to ensure trimmed flight and controllability.

A comparison of the optimized structures between the midpoint and best candidate designs is presented in Figures 10 and 11.

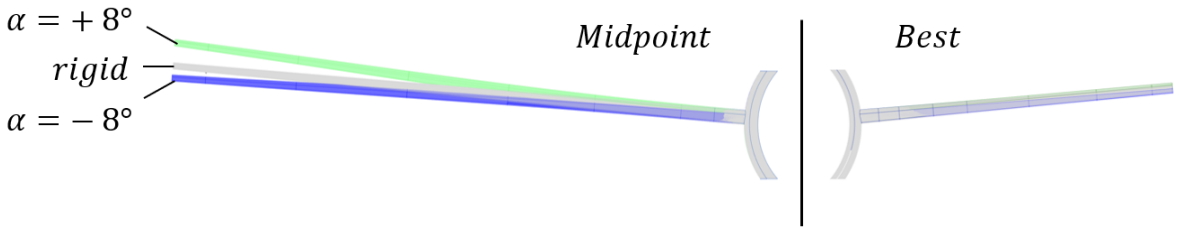



Figure 10 – Comparison of the wing structure deformation between the optimized wing structure of the midpoint and best candidate under the envelope load cases of $\alpha = 8°$ (green), $\alpha = -8°$ (blue), and the rigid shape (gray).

The wing deflection under the envelope aerodynamic load cases at $\alpha = \pm 8°$ shows a maximum tip deflection of 3.5 % halfspan for the midpoint design, whereas the deflection of the best candidate design is barely visible at less than 0.4 %. A possible wash-out effect from the structural deformation back to the aerodynamic loads is therefore also negligible for this specific unswept, low aspect-ratio wing design.

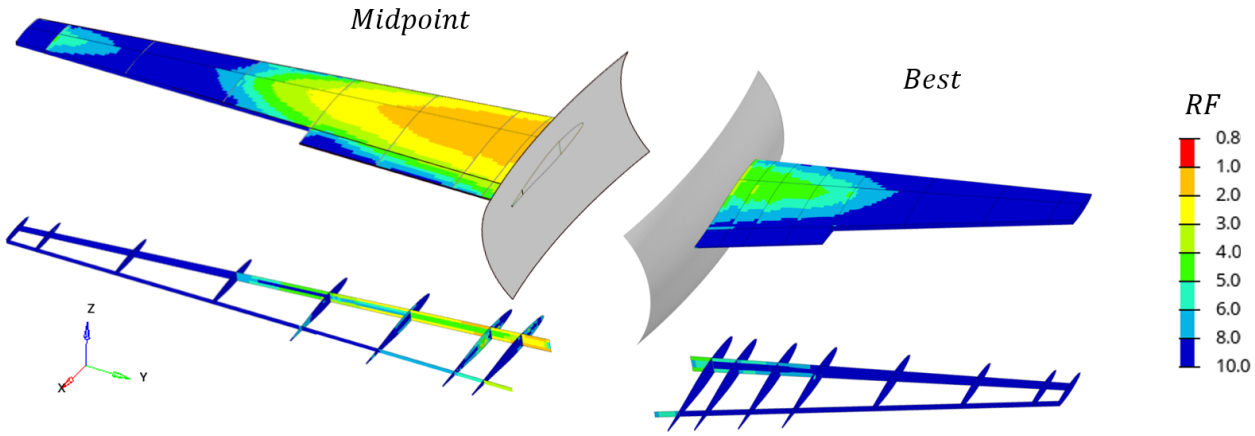



Figure 11 – Comparison of the reserve factor $RF$ for the optimized wing structures of the midpoint design versus the best candidate under the envelope load cases of $\alpha = \pm 8°$, all above unity.

Although the minimum reserve factors $RF$ of the midpoint design are closer to unity than those of the best candidate, the optimizer drives the thickness of all elements down to the lower bound, which was set to $t_{min} = 0.4\,\mathrm{mm}$ as a manufacturing constraint. The lowest reserve factors are located in the inboard wing skins and the upper and lower caps of the forward spar.

Based on the optimization results, a sensitivity study on the mass prediction capability was performed. The analytical square-cube law (SQL) as applied to the OTIFAN configuration in [9] is given by Eq. 9:

$$\left(\frac{m}{m_{min}}\right) = \left(\frac{b - d_f}{b_{min} - d_f}\right)^k \quad where \quad k = 1.4 \tag{9}$$

This scaling law relates the mass scaling to a span scaling, corrected for the local fuselage diameter. The component masses at the current and minimum spans, $b$ and $b_{min}$, are denoted as $m$ and $m_{min}$, respectively. The parameter $d_f$ denotes the fuselage diameter at the root of the corresponding lifting surface.

The results of the mass sensitivity study with respect to the wing span are presented in Figure 12. As indicated in light blue, for wing span values in the range of $b_w \leq 1.0\,\mathrm{m}$ LAGRANGE drives the thickness of the entire wing structure down to the manufacturing constraint of $t_{min} = 0.4\,\mathrm{mm}$, resulting in an initially linear mass increase. For wing span values $b_W > 1.0\,\mathrm{m}$ the LAGRANGE mass increase shows similarity to the exponential SQL method, albeit an offset remains. The potential mass savings achieved by the new method on the total aircraft mass ranges from 5 % to 29 %, directly improving multi-mission performance. Specifically, a significant objective increase of 17 points is observed for the midpoint design.

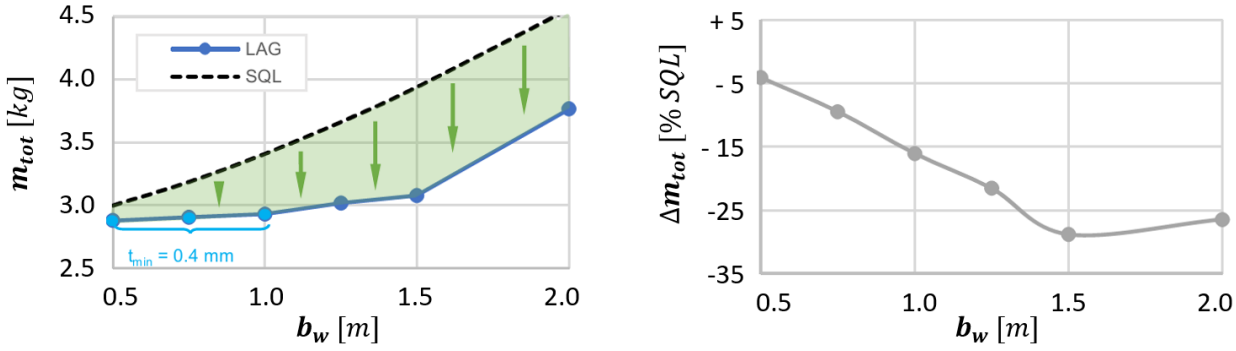



Figure 12 – Mass scaling study comparing the structural optimization results from the structural optimizer LAGRANGE versus the analytical SQL method.

## 4. Conclusion & Outlook

In this study, a high-fidelity, dataset-based shape and structure optimization framework was demonstrated on the Optimization Test Interceptor with ducted fan (OTIFAN). The framework includes a unidirectional structural optimization loop for the primary load-bearing component, the wing.
This enhanced structural modeling replaces empirical or analytical mass estimations with a detailed finite element model sized directly against high-fidelity, rigid aerodynamic loads and it accounts for panel-buckling via a global knockdown factor. The evaluated load cases comprehensively cover the operational flight envelope of the vehicle, including challenging off-design regions characterized by post-stall aerodynamics and control surface power saturation.
Ultimately, this integrated approach enables aircraft designers to evaluate mission performance - which is inherently sensitive to the mass properties - with significantly higher fidelity and predictive confidence.
For the test case of an agile unmanned aerial interceptor, the total vehicle mass estimate was reduced by 5 % to 29 % versus the analytical estimation, significantly increasing the predicted mission performance. The best candidate furthermore displays negligible deformation of the external shape at zero aileron deflection, rendering the unidirectional fluid-structure interaction (FSI) between aerodynamics and structural mechanics a viable approach for sizing of this low-aspect ratio configuration.

Future investigations on the sensitivity to panel-buckling and the implications thereof among further constraints could potentially unlock further structural mass savings, or increase the level of trustworthiness in the sizing result, as the current framework is restricted by a conservative global knockdown factor. Based on this promising demonstration, future work may furthermore expand the range of aircraft components included in the sizing loop, eventually transitioning toward a holistic, global finite element model (GFEM) of the complete aircraft configuration.

## Contact Author Email Address

Mailto: markus.v.maier@tum.de

## Copyright Statement

The authors confirm that they, and/or their company or organization, hold copyright on all of the original material included in this paper. The authors also confirm that they have obtained permission, from the copyright holder of any third party material included in this paper, to publish it as part of their paper. The authors confirm that they give permission, or have obtained permission from the copyright holder of this paper, for the publication and distribution of this paper as part of the ICAS proceedings or as individual off-prints from the proceedings.

## Acknowledgements

The funding of the activities by Airbus Defence & Space GmbH (www.airbus.com) and the scientific guidance by the Chair of Aerodynamics and Fluid Mechanics at the Technical University of Munich (AER, www.epc.ed.tum.de/aer) is gratefully acknowledged. The authors want to thank the German Aerospace Center (DLR, www.dlr.de/en) for providing the computational fluid dynamics solver TAU, Airbus Defence & Space GmbH for providing additional software frameworks as well as the Gauss Centre for Supercomputing e.V. (GCS, www.gausscentre.eu) for funding this project by providing computing time on the Linux Cluster and the SuperMUC NG at Leibniz Supercomputing Center (LRZ, www.lrz.de).

## References

[1] Jun-xue Leng, Zhen-guo Wang, Wei Huang, Yang Shen, and Kai An. Multidisciplinary design optimization processes for efficiency improvement of aircraft: State-of-the-art review. *International Journal of Aeronautical and Space Sciences*, 26(4):2020–2042, July 2025.

[2] Arthur Rizzi and James M. Luckring. Historical development and use of cfd for separated flow simulations relevant to military aircraft. *Aerospace Science and Technology*, 117:106940, 2021.

[3] Matteo Moioli, Christian Breitsamter, and Kaare A. Sørensen. Turbulence modeling for leading-edge vortices: an enhancement based on experimental data. In *AIAA Scitech 2020 Forum*, Orlando, FL, January 2020. American Institute of Aeronautics and Astronautics.

[4] Kaare Sørensen-Libik. Overview and results of subproject vitamin-abc. In Ralf Heinrich, editor, *Advanced Aircraft Understanding via the Virtual Aircraft Model*, volume 155 of *Notes on Numerical Fluid Mechanics and Multidisciplinary Design*, page 123 ff. Springer Nature Switzerland AG, 2025.

[5] Kjell Bramsiepe, Arne Voß, and Thomas Klimmek. Design and sizing of an aeroelastic composite model for a flying wing configuration with maneuver, gust, and landing loads. *CEAS Aeronautical Journal*, 11(3):677–691, Sep 2020.

[6] Christopher Reinbold, Christian Breitsamter, and Kaare A. Sørensen. Aeroelastic dataset generation using cfd-csm simulations with a chimera approach for control surfaces. In *AIAA SCITECH 2022 Forum*, San Diego, CA, January 2022. American Institute of Aeronautics and Astronautics.

[7] Fabian Volle. Aero-structural optimization of the aiaa mdo benchmark model with tau and lagrange. In *AIAA SCITECH 2025 Forum*, Orlando, FL, January 2025. American Institute of Aeronautics and Astronautics.

[8] G. Schuhmacher, F. Daoud, O. Petersson, and M. Wagner. Multidisciplinary airframe design optimization. In *Proceedings of the 28th ICAS Congress*, Brisbane, Australia, September 2012. ICAS.

[9] Markus Maier, Kaare Sørensen-Libik, and Christian Breitsamter. Robust high-fidelity dataset-based shape optimization for aircraft design. *Aerospace Science and Technology*, page 112465, 2026.

[10] Ming Li, Junqiang Bai, Li Li, Xiaoxuan Meng, Qian Liu, and Bao Chen. A gradient-based aero-stealth optimization design method for flying wing aircraft. *Aerospace Science and Technology*, 92:156–169, 2019.

[11] Abdelkader Benaouali and Stanisław Kachel. Multidisciplinary design optimization of aircraft wing using commercial software integration. *Aerospace Science and Technology*, 92:766–776, 2019.

[12] Alasdair C. Gray, Graeme Kennedy, and Joaquim R. Martins. Geometrically nonlinear high-fidelity aerostructural optimization including geometric design variables. In *AIAA AVIATION 2023 Forum*, San Diego, CA, June 2023. American Institute of Aeronautics and Astronautics.

[13] Melike Nikbay, Sihmehmet Yildiz, Berkay Pirlepeli, and Konstantinos Kontis. Multidisciplinary design optimization of a non-planar flying wing ucav concept. *Aerospace Science and Technology*, 177:112285, 2026.

[14] Aiden L. Gray and David W. Zingg. Blended-wing-body regional aircraft optimization with high-fidelity aerodynamics and critical design requirements. *Journal of Aircraft*, 61(6):1775–1792, 2024.

[15] Mohammad Abu-Zurayk, Antoine DeBlois, Joël Brezillon, Ben D. Phillips, Ögmundur Petersson, Raul llamas, Časlav Ilić, Eliot Aretskin-Hariton, Jeffryes W. Chapman, Patrick Wegener, Jan Himisch, Matthias Schulze, Jannik Häßy, Sascha Dähne, Cian Conlan-Smith, Jasveer Singh, Sebastian Wöhler, Christophe Blondeau, Michael Meheut, Sven Geisbauer, and Stefan Görtz. Establishing a joint research-industry MDO benchmark based on the DLR-F25 aircraft configuration. In *AIAA SCITECH 2026 Forum*, Orlando, FL, January 2026. American Institute of Aeronautics and Astronautics.

[16] Kaare A. Sørensen, Udo Tremel, Herbert Rieger, and Stephan M. Hitzel. Simulation of manoeuvring fighter aircraft with the unstructured chimera approach. In *45th AIAA Aerospace Sciences Meeting and Exhibit*, Reno, NV, January 2007. American Institute of Aeronautics and Astronautics. DOI: 10.2514/6.2007-123.

[17] Dieter Schwamborn, Thomas Gerhold, and Ralf Heinrich. The DLR TAU-code: Recent applications in research and industry. In *Proceedings of the European Conference on Computational Fluid Dynamics (ECCOMAS CFD 2006)*, Egmond aan Zee, The Netherlands, September 2006. TU Delft.

[18] Christopher Reinbold. *Aeroelastic Dataset Generation and Analysis Based on Coupled CFD-CSM Simulations and a Chimera Approach for Control Surface Deflections*. PhD thesis, Technische Universität München, 2025.

[19] Philippe R. Spalart and Steven R. Allmaras. A one-equation turbulence model for aerodynamic flows. In *30th Aerospace Sciences Meeting and Exhibit*, Reno, NV, January 1992. American Institute of Aeronautics and Astronautics.

[20] MakeItFrom.com. Material properties database. `https://makeitfrom.com`, 2026. Accessed: June 9, 2026.